JACS
JOURNAL OF THE AMERICAN CHEMICAL SOCIETY

pubs.acs.org/JACS

Article

Active-Site Modulation in an Fe-Porphyrin-Based Metal–Organic Framework through Ligand Axial Coordination: Accelerating Electrocatalysis and Charge-Transport Kinetics

Itamar Liberman,[†] Ran Shimoni,[†] Raya Ifraemov, Illya Rozenberg, Chanderpratap Singh, and Idan Hod*

Cite This: *J. Am. Chem. Soc.* 2020, 142, 1933–1940

Read Online

ACCESS | Metrics & More | Article Recommendations | Supporting Information

ABSTRACT: The construction of artificial solar fuel generating systems requires the heterogenization of large quantities of catalytically active sites on electrodes. In that sense, metal–organic frameworks (MOFs) have been utilized to assemble unpreceded concentration of electrochemically active molecular catalysts to drive energy-conversion electrocatalytic reactions. However, despite recent advances in MOF-based electrocatalysis, so far no attempt has been made to exploit their unique chemical modularity in order to tailor the electrocatalytic function of MOF-anchored active sites at the molecular level. Here, we show that the axial coordination of electron-donating ligands to active MOF-installed Fe-porphyrins dramatically alters their electronic properties, accelerating the rates of both redox-based MOF conductivity and the electrocatalytic oxygen reduction reaction (ORR). Additionally, electrochemical characterizations show that in multiple proton-coupled electron transfer reactions MOF-based redox hopping is not the only factor that limits the overall electrocatalytic rate. Hence, future efforts to enhance the efficiency of electrocatalytic MOFs should also consider other important kinetic parameters such as the rate of proton-associated chemical steps as well as mass-transport rates of counterions, protons, and reactants toward catalytically active sites.

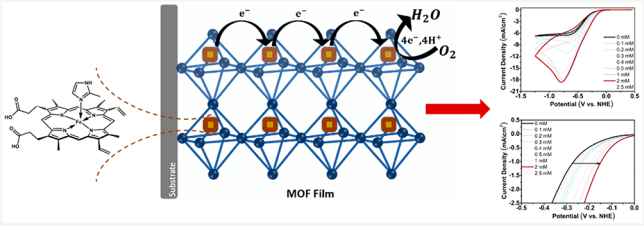

INTRODUCTION

Metal organic frameworks (MOFs),[1,2] a crystalline, porous subclass of coordination polymers, have stimulated significant interest in the scientific community over the last two decades due to their exceptional properties as high surface area and porosity, well-defined crystallinity, and unique chemical and physical modularity.[1,3−7] Therefore, MOFs are being used in a wide variety of applications as gas storage/separation,[8,9] chemical catalysis,[10−12] sensing,[13] and photocatalysis.[14,15] Over the last few years, attention has also been given to develop new schemes for electrocatalysis[16−23] and artificial photosynthesis[24−30] which are based on MOFs. In principle, much like catalytic enzymes, electrocatalytic MOFs could potentially incorporate all of the functional elements needed for efficient catalysis: (1) the ability to immobilize an unparalleled number of catalytic sites;[31] (2) the inclusion of mass-transport channels in contrast to dense, bulk inorganic, or polymeric films, where only a small fraction of the material is solution-accessible (and thus catalytically active); an MOF creates an ordered, porous heterogeneous network that allows the electrolyte species and catalytic substrates to permeate the interior of the film;[15,18,32,33] (3) separation between charge-transporting and catalytic moieties by the addition of shuttles to deliver redox equivalents to and from the MOF-tethered catalytic sites; and (4) modulation of the catalyst secondary chemical environment.[31]

Indeed, over the last years several examples of successful heterogenization of a high concentration of molecular catalysts in MOFs were presented,[18,20] showing the ability to drive important electrocatalytic reactions as hydrogen evolution, CO_2 reduction,[34,35] water oxidation, and oxygen reduction. For these electrocatalytic MOFs, it has been shown that redox conductivity constitutes a kinetic bottleneck impeding the overall catalytic performance of the system. As a consequence, a number of different approaches were suggested to overcome this obstacle, including (a) π-stackings of MOF-based linkers and incorporated conductive guests;[36−38] (b) the delocalization of the charge in 2D MOFs;[39] (c) charge transport through MOF-installed conductive polymers;[40] and (d) conduction through a redox hopping mechanism between spatially isolated redox-active moieties (MOF nodes or linkers).[41−45]

Yet, so far to the best of our knowledge, no attempt has been made to exploit the exceptional chemical modularity of MOFs for electrocatalysis in order to precisely tune and manipulate the catalytically active site's properties. In that sense, for biological enzymatic systems it is well known that molecular

Received: October 22, 2019
Published: January 7, 2020

https://dx.doi.org/10.1021/jacs.9b11355
J. Am. Chem. Soc. 2020, 142, 1933–1940

moieties residing in the surroundings of the active site can greatly influence the catalytic activity. For instance, in naturally occurring oxygen utilization reactions, the axial coordination of electron-donating ligands as imidazole and histidine is used to control the function of the Fe-porphyrin catalytic sites.[46]

In this work, we demonstrate that the electronic properties of MOF-anchored Fe-porphyrins could be systematically tailored via axial coordination of an electron-donating ligand, 2-methylimidazole (MeIM), to the active metal site. Due to the chemical and structural robustness of Zr_6-oxo-based MOFs, as a model system we have chosen to explore an Fe-porphyrin (Hemin)-modified UIO-66 (termed UIO-66@Hemin) for an electrocatalytic oxygen reduction reaction (ORR). We found that the effect of MeIM axial coordination is 2-fold: (i) it serves as a powerful tool to boost the ORR catalytic rates, increasing catalytic currents by a factor of 2.9 while anodically shifting the onset potential by 124 mV and (ii) it enhances the kinetics of charge hopping between adjacent redox-active Fe-porphyrin sites. Moreover, electrocatalytic analysis conducted under hydrodynamic convection conditions revealed that the rate of a single redox hopping event (extracted under noncatalytic conditions) is not the sole parameter that dictates the overall electrocatalytic rate of the MOF-based system. In complex proton-coupled electron transfer reactions (such as ORR), the completion of a catalytic cycle requires multiple hopping events/chemical steps while the effect of mass-transport kinetics (counterions, protons, and catalytic reactants in both the bulk electrolyte and inside the MOF's pores) should also be taken into account.

RESULTS AND DISCUSSION

In order to obtain UIO-66@Hemin, first a UIO-66 MOF having a high density of defect sites (missing linkers) was synthesized according to a previously reported procedure.[47,48] Briefly, 1 mL of hydrochloric acid was included in the reaction solution to accelerate the rate of MOF crystallization, hence forming a large concentration of undercoordinated Zr_6-oxo MOF nodes (defect sites). In turn, these formed defect sites serve as tethering spots for Hemin immobilization via postsynthetic solvent-assisted ligand-incorporation (SALI),[49] as can be seen in Scheme 1a.

Powder X-ray diffraction (PXRD) confirms the successful synthesis of UIO-66 as well as the preservation of MOF crystallinity upon Hemin anchoring (Figure S1).[48,50,51] In addition, scanning electron microscopy (SEM) images show the retention of crystal size and morphology upon Hemin modification (Figure S2). Inductively coupled plasma-atomic emission spectroscopy (ICP-AES) measurements show that for UIO-66@Hemin the Zr_6-oxo node to Hemin ratio is 4:1 (Table S1). N2 physisorption measurements show similar surface areas for UIO-66 and UIO-66@Hemin (1557 and 1594 m^2/gr, respectively), in accordance with previous reports on the defective UIO-66 surface area (Figure S3a).[48,52] As shown in Figure S3b, pore size distribution analysis reveals a slight decrease in average pore width for UIO-66@Hemin compared to UIO-66 due to the installation of the catalyst in the MOF pores.[48] In addition, to calculate the defect-site density in UIO-66 and UIO-66@Hemin, we combined nuclear magnetic resonance (^{1}H NMR)[52] and ICP-AES (Figure S4). First, ^{1}H NMR measurements were taken in order to quantify the number of BDC linkers in UIO-66 and UIO-66@Hemin MOFs. In addition, ICP-AES measurements were conducted to analyze the concentration of Zr_6-based nodes in the MOFs.

Scheme 1. Illustration of the UIO-66@Hemin Structure[a]

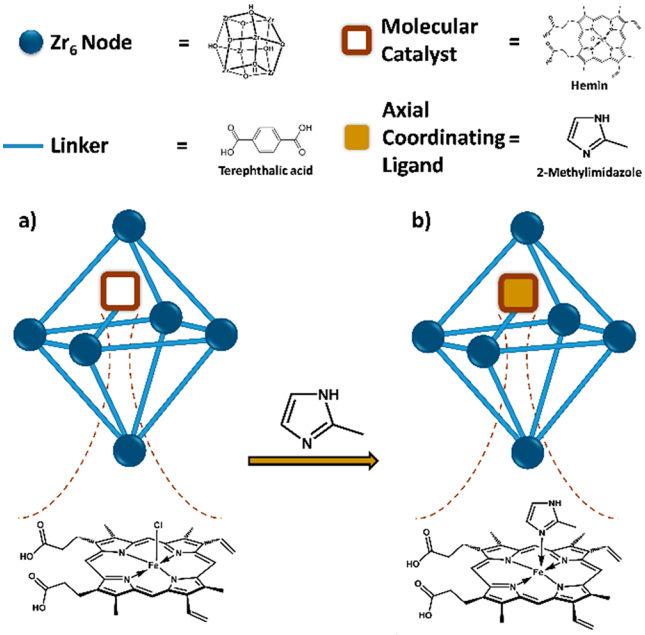

[a](a) Defective UIO-66 functionalized with the Hemin molecular catalyst. (b) MeIM axial coordination to UIO-66@Hemin.

Thus, by combining both results, we were able to extract the Zr_6-to-BDC ratio and hence quantitively detect the density of defect sites (missing linkers). For both UIO-66 and UIO-66@Hemin, we obtained ∼9 BDC linkers per node (Figure S4b), meaning that our MOFs indeed contain significant numbers of defects. (Fully saturated UIO-66 contains 12 BDC linkers per node.) Confirmation of Hemin tethering to the Zr_6-oxo MOF node was obtained through Raman spectroscopy (Figure S5). For UIO-66 two peaks appear at 1432 and 1447 cm^{-1}, attributed to in-phase carboxylate (OCO) symmetric stretching of the BDC linkers. For UIO-66@Hemin, the relative intensity of both bands is significantly attenuated due to Hemin-based OCO stretching, indicating successful Hemin anchoring to the MOF's node.[53]

In order to monitor the MeIM axial coordination to UIO-66@Hemin (Scheme 1b), we have thoroughly characterized our samples using Raman spectroscopy, electron paramagnetic resonance (EPR), and X-ray photon electron spectroscopy (XPS). Raman spectroscopy is known to be sensitive to the electronic and structural properties of porphyrins through the ν_2- and ν_4-symmetric pyrrole stretching bands.[54] As can be seen in Figure S6, MeIM axial coordination to UIO-66@Hemin can be followed by comparing the changes in ν_2 and ν_4 bands. Specifically, upon axial ligation, we observe a shift of ν_2 toward higher frequencies (from 1369 to 1372 cm^{-1}), indicating the conversion of low-spin Fe^{3+}-Hemin to a high-spin species (Figure S6b). Additionally, ν_4 bands of both high- and low-spin states are observed (1568 and 1554 cm^{-1}, respectively), but upon MeIM coordination, the relative intensity of the high-spin band is enhanced (Figure S6c). Further confirmation of MeIM coordination to UIO-66@Hemin is obtained via EPR analysis (Figure S7), showing a significant shift in the g_x signal (g_x = 6.57) in comparison to that of noncoordinated UIO-66@Hemin (g_x = 6.15) due to a change in Hemin's electronic configuration.[55] Moreover, the N 1s XPS of MeIM-coordinated UIO-66@Hemin reveals the

https://dx.doi.org/10.1021/jacs.9b11355
J. Am. Chem. Soc. 2020, 142, 1933−1940

existence of both pyrrole-based (at 398.4 eV) and imidazole-based NH^+ (at 401.1 eV) species (Figure S8).[56]

Thereafter, the effect of MeIM axial coordination on the electrochemical activity of UIO-66@Hemin was examined. Thin films of UIO-66@Hemin were deposited on a conductive carbon cloth electrode using an ink drop-casting method. (See the Supporting Information for experimental details.) Cyclic voltammetry (CV) measurements were conducted with a standard three-electrode setup containing a Pt counter and a Ag-based quasi-reference electrode (referenced against the $Fc^{+/0}$ redox couple) in 0.1 M $LiClO_4$ acetonitrile (MeCN) electrolyte (with varying concentrations of MeIM) under an inert Ar atmosphere. As can be seen in Figure 1a, regardless of the presence of MeIM in solution, all UIO-66@Hemin samples exhibit quasi-reversible redox activity corresponding to the Hemin-based $Fe^{3+/2+}$ couple, yet upon MeIM axial coordination to Hemin, a clear cathodic shift in the formal redox potential is observed (coupled with a decrease in peak separation), thus indicating the modulation of Hemin's electronic properties by the axial coordination. The extent of the cathodic shift can be easily seen through monitoring the change in the cell's open-circuit potential (Figure 1b). Up to an MeIM concentration of 0.5 mM, a cathodic shift of more than 120 mV is observed, while at higher concentration there is no further change in Hemin's redox potential, possibly due to axial coordination to all electroactive Hemins. Typically, upon axial ligation of MeIM, the redox potential will shift according to the difference in the MeIM binding constant to Fe^{2+} and Fe^{3+}. Thus, generally for Fe-porphyrins (where Fe^{2+} binds more strongly to MeIM) one should expect an anodic shift in the redox potential. However, it is well known that in the case of a porphyrin system that has steric hindrance toward MeIM binding (such as our MOF-based system which contains an anchored Hemin within small cavities of about 1 nm), a cathodic shift is often observed.[57]

The electrochemical activity of MOF-immobilized Hemins (as opposed to the case of freely diffusing homogeneous Fe-porphyrins) is largely affected by the propagation of charge through hopping between neighboring redox-active sites. Consequently, we were interested in understanding how the observed electronic tuning of MOF-tethered Hemins (through MeIM axial coordination) alters the kinetics of charge transport in our UIO-66@Hemin films. To do so, potential-step chronoamperometry measurements were recorded to determine the rates of charge hopping between neighboring Hemin-based ligands in the MOF films. We stepped the potential from 0.15 V vs $Fc^{+/0}$ (Fe^{3+} state in all Hemins) to −0.45 V vs Fc/Fc^+ (Fe^{2+} state in all Hemins). The resulting current transients were analyzed using the Cottrell equation[58]

$$I(t) = \frac{(nFACD_{\text{hopping}}{}^{1/2})}{(\pi^{1/2}t^{1/2})}$$

where n is the number of electrons transferred per hopping event (1 for the Hemin-based $Fe^{3+/2+}$ couple), F is the Faraday constant, A is the geometrical area of the MOF working electrode (1 cm^2), C is the molar concentration of the redox-active Hemin molecules in the film (0.167 mol/cm^3), and D_{hopping} is the diffusion coefficient (in cm^2/s). On short-enough measurement time scales, where the diffusion obeys semi-infinite conditions, $I(t)$ vs $t^{-1/2}$ behaves linearly (Figure S9), and one can extract the value of D_{hopping} from the curve's slope. The redox hopping rate, k_{hopping} (s^{-1}), is related to the extracted D_{hopping} by the term

$$k_{\text{hopping}} = \frac{D_{\text{hopping}}}{r^2}$$

where r is defined as the distance (cm) between two adjacent redox-active Hemin moieties (estimated to be 2.9 nm, see Figure S10). Figure 1c and Table S2 show the obtained k_{hopping} as a function of MeIM concentration. Interestingly, k_{hopping} indeed exhibits a clear dependency on the extent of MeIM

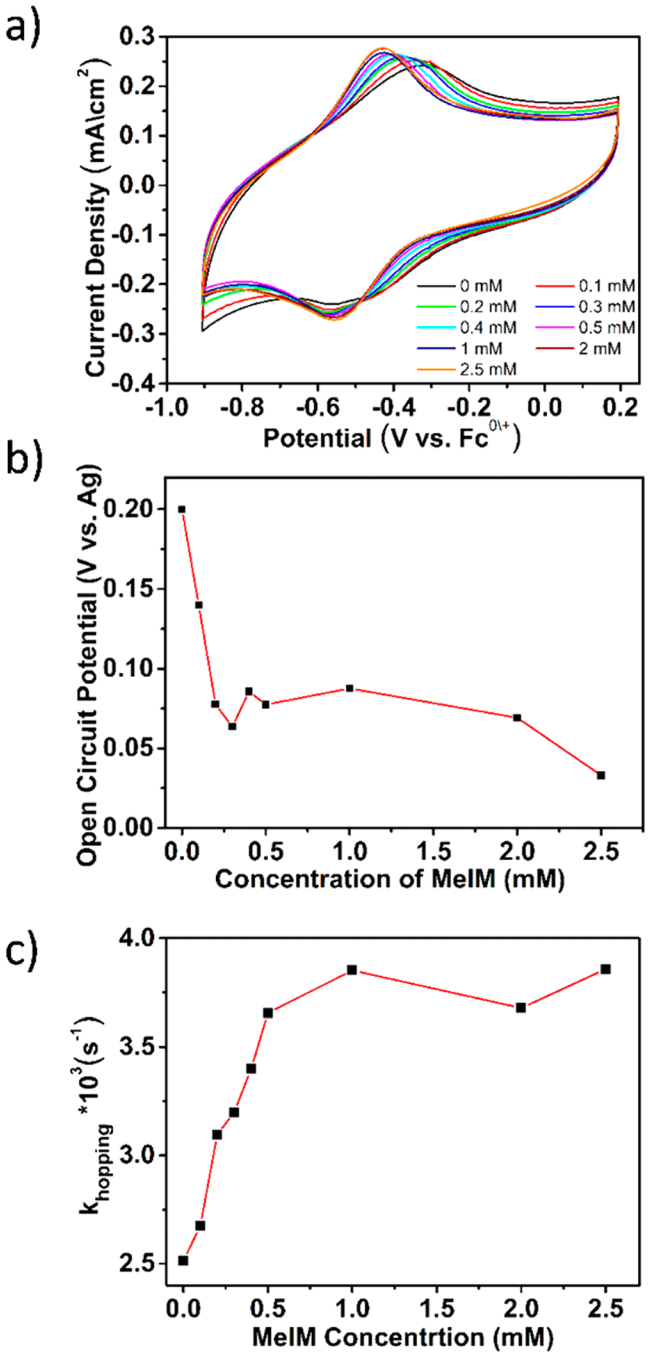

Figure 1. (a) CVs of UIO-66@Hemin with different solution concentrations of MeIM (0−2.5 mM), conducted in an Ar environment at a scan rate of 100 mV/s. (b) Electrochemical open circuit potential as a function of MeIM concentration. (c) D_{hopping} of UIO-66@Hemin as a function of MeIM concentration.

https://dx.doi.org/10.1021/jacs.9b11355
J. Am. Chem. Soc. 2020, 142, 1933−1940

axial coordination to the MOF-anchored Hemins. In fact, $k_{hopping}$ could be systematically enhanced from 2513 s^{-1} for 0 mM MeIM to 3858 s^{-1} for 2 mM MeIM (a 53% increase in redox hopping rates).

Next, we were interested in disclosing the effect of MeIM axial coordination on UIO-66@Hemin's electrocatalytic properties. Homogeneous Fe-porphyrin is a well-known active molecular catalyst for the electrocatalytic oxygen reduction reaction (ORR).[59] Moreover, for these homogeneous catalysts, the axial coordination of electron-donating ligands increases the rate of ORR via the "push" mechanism.[60,61] Specifically, during electrocatalytic ORR, the reduction of [Fe^{III}–porphyrin]$^+$ forms an Fe^{II}(porphyrin) species that is able to effectively bind O_2 (via electron donation) to form the ORR intermediate, Fe^{III}(porphyrin)($O_2^{\bullet-}$).[62] The affinity of O_2 for the Fe^{II}(porphyrin) species could be tuned by manipulating the metal's electronic properties. A promising route to do so is by the axial coordination of electron-donating ligands (such as MeIM) to the active metal site. In that manner, one can increase the electron density at the Fe site, thus lowering the barrier for electron transfer to form the catalyst-bound superoxide ($O_2^{\bullet-}$) and thus boost the overall ORR performance.

Hence, we set out to examine the ORR activity of our system. To do so, thin films of UIO-66@Hemin were drop-cast on a glassy carbon rotating ring-disk electrode (RRDE). (See the Supporting Information for experimental details.) Electrochemical measurements were performed in a gas-tight three-electrode setup containing UIO-66@Hemin films as the working electrode, an Ag wire quasi-reference electrode, and a Pt foil counter electrode in 0.1 M $LiClO_4$ MeCN containing 10% H_2O (the proton source for ORR). Figure 2a presents CVs of UIO-66@Hemin (scan rate of 100 mV/s) with different concentrations of MeIM (0–2.5 mM) in an oxygen environment. For all samples, a clear ORR catalytic peak is observed at potentials corresponding to the Hemin $Fe^{3+/2+}$ redox couple. Remarkably, by varying the concentrations of MeIM one could systematically tune the resulting ORR catalytic rates. As summarized in Figure 2b, catalytic currents are enhanced by ~290%, from −6.44 mA/cm^2 up to −18.59 mA/cm^2 for 0 and 2 mM MeIM, respectively. (At higher MeIM concentrations, catalytic currents essentially remain constant.) Additionally, as can be seen in Figure 2c,d, the ORR onset potential (termed the potential needed to drive a catalytic current of 1 mA/cm^2) is also tuned by the extent of axial coordination to the Hemin. By increasing the MeIM concentration, a gradual anodic shift in the onset potential is observed, reaching a maximum of 124 mV at 2 mM MeIM. On the contrary, a control bare UIO-66 film (without installed Hemin catalysts) shows significantly diminished activity (in terms of both catalytic currents as well as the onset potential), and as expected, no apparent effect is observed in the presence of MeIM in electrolyte (Figure S11). Furthermore, the electrocatalytic ORR activity of homogeneous Hemin was characterized in an O_2-saturated 0.1 M $TBAPF_6$ DMF electrolyte containing 10% H_2O (Figure S12). As expected, homogeneous Hemin exhibits clear ORR activity at potentials corresponding to the $Fe^{3+/2+}$ couple. Additionally, in the presence of a large excess of MeIM (8 mM), a similar enhancement in ORR activity is observed (increased catalytic current coupled to the anodic shift of the reaction's onset potential), albeit to a lesser extent. Hence, these results confirm that Hemin is responsible for the measured ORR activity in our MOF.

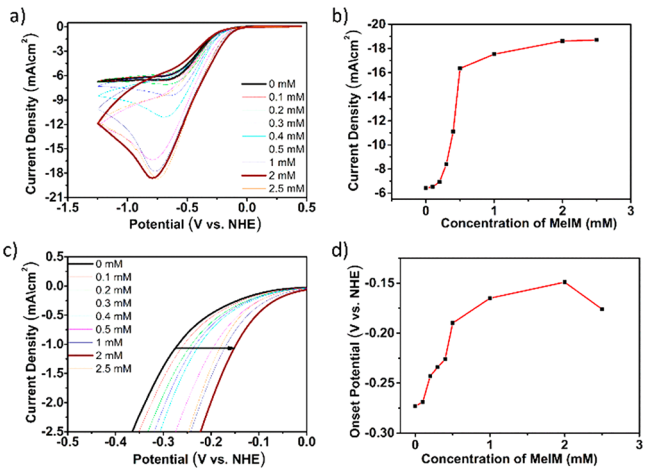

Figure 2. Comparison of UIO-66@Hemin ORR performance as a function of MeIM solution concentration (0–2.5 mM). (a) CV conducted in O_2 environments (scan rate of 100 mV/s). (b) A plot of ORR electrocatalytic peak current. (c) Electrocatalytic ORR onset potential (defined as the potential needed to drive an ORR current of 1 mA/cm^2). (d) Plot presenting the systematic change in catalytic onset potential as a function of MeIM concentration. Measurements conducted using a glassy carbon electrode (diameter = 0.3 cm, MOF surface loading of 30 μg).

In order to evaluate the ORR product selectivity of UIO-66@Hemin as a function of MeIM concentration, an RRDE electrochemical analysis was performed. As can be seen in Figure S13, linear sweep voltammetry (LSV) measurements were obtained for all samples by scanning the potential of a UIO-66@Hemin disc electrode cathodically (in order to reduce oxygen), while the Pt-based ring electrode was held constant at a potential of 0.75 V vs NHE to oxidize the ORR-formed H_2O_2 product (RRDE was rotated at 1600 rpm to avoid any limitation of H_2O_2 mass transport toward the ring electrode). As a result of this characterization, for all applied potentials, we were able to extract both the portion of H_2O_2 produced during ORR and the average number of transferred electrons per catalytic cycle (Figure S14). All samples produce only trace amounts of H_2O_2 (less 2%) and exhibit essentially four transferred electrons, thus implying the high product selectivity toward the H_2O of UIO-66@Hemin regardless of MeIM axial coordination. As shown in Figures S15 and S16, the ORR selectivity of a bare UIO-66 film was also analyzed, showing significantly lower product selectivity (up to 30% H_2O_2 production).

The stability of the best-performing system (UIO-66@Hemin with 2 mM MeIM) was monitored through a 7 h electrolysis test conducted at −0.45 V vs NHE (Figure S17a). Due to the low O_2 solubility in MeCN, during prolonged catalytic conditions O_2 was depleted in the vicinity of the catalytic sites, and thus a decline in catalytic currents was observed. As a result, to ensure that the electrolyte remains O_2-saturated, every 30 min of electrolysis was followed by a 10 min O_2-purging period. Notably, it is clearly seen that UIO-66@Hemin preserves its ORR activity for about 4 h. Nevertheless, for a longer electrolysis duration, one can observe a slow decay in catalytic performance. As seen in Figure S17b, Raman spectroscopy of an UIO-66@Hemin film before and after electrolysis reveals at least a partial

https://dx.doi.org/10.1021/jacs.9b11355
J. Am. Chem. Soc. 2020, 142, 1933–1940

preservation of the Hemin-based active site (Hemin-based pyrrole stretching bands remained essentially unchanged). In addition, SEM images show the retention of the MOF's crystal morphology during electrolysis (Figure S17c,d).

By now we know that in UIO-66@Hemin systems axial coordination of MeIM to the active MOF-installed Hemins modulates its electronic nature and consequently boosts the rates of both charge hopping and overall ORR electrocatalysis. In an effort to further understand the operation mechanisms governing electrocatalysis in our MOF-based system, we set out to determine the ORR kinetic rate constants by carrying out rotating disk electrode (RDE) voltammetry experiments at varying rotation speeds. When measuring LSVs under convection conditions, catalytic currents follow the Koutecky–Levich relation[63]

$$\frac{1}{I_{lim}} = \underbrace{\frac{1}{nFAk\Gamma C_b}}_{a} + \underbrace{\frac{1}{0.62nFA\nu^{1/6}D^{2/3}\omega^{1/2}C_b}}_{b}$$

where C_b is the bulk concentration of the catalytic substrate in solution (1.5 mM for O_2 at saturation), Γ is the catalyst's total surface coverage (5×10^{-8} mol/cm^2), ν is the solution's kinematic viscosity, ω is the rate of rotation (rad/s), F is the Faraday constant, A is the surface area of the electrode, n is the number of electrons transfered in one catalytic event (four for ORR in our system), D is the diffusion constant, and k is the first-order catalytic rate constant (in M^{-1} s^{-1}). Pseudo 0-order rate constant k_{cat} (s^{-1}) could be obtained by multiplying k by C_b. Looking at the Koutecky–Levich equation, the a parameter corresponds to the maximum rate at which O_2 is converted to H_2O within the MOF, while the b parameter signals the rate of O_2 arrival at the outer boundary of the MOF film. Thus, plotting $1/I_{lim}$ vs $1/\omega^{1/2}$ and extrapolating the intercept (infinite rotation rate, eliminating mass-transport effects) allows us to distinguish between the MOF-electrode related rate-limiting steps and solution-based diffusion limitation and extract the catalytic rate constant, k_{cat}.

Consequently, to determine the effect of MeIM axial coordination on the intrinsic ORR activity of UIO-66@Hemin, we have calculated k_{cat} as a function of applied potential for two samples: 0 and 2 mM MeIM (Figure 3). To do so, for each sample a series of LSVs were recorded at varying rotation speeds (100–3000 rpm). For each applied potential, intercepts of the catalytic current were extrapolated and used to calculate k_{cat} (Tables S3). Figure 3 highlights several important insights. First, throughout the entire potential range, the addition of 2 mM MeIM enhances k_{cat} by a factor of about 1.5, thus indicating the direct effect of axial coordination on the intrinsic activity of MOF-installed Hemins. Second, both samples possess similar linear slopes, shifted from one another by more than 100 mV, comparable to the obtained shift in catalytic onset potentials. Third, for both samples (regardless of the MeIM axial coordination) k_{cat} reaches saturation at a certain potential threshold, meaning that at these potentials the overall ORR rate is limited by factors other than the intrinsic catalysis rate at the Hemin active site.

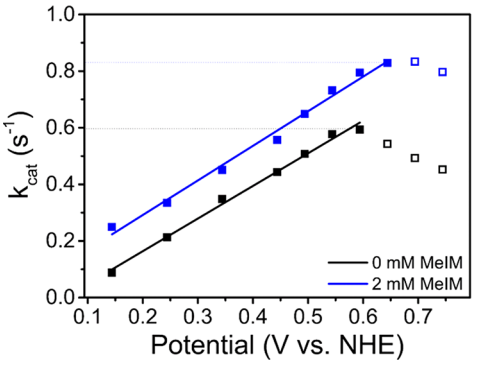

Figure 3. (a) Comparison of extracted ORR k_{cat} for UIO-66@Hemin, with (2 mM) and without MeIM axial coordination, as a function of applied potential.

In that regard, it is often assumed that redox-based charge hopping is the sole rate-limiting step in MOF-based electrocatalytic systems. Yet, for UIO-66@Hemin, potential-step-determined $k_{hopping}$ values are about 3 orders of magnitude higher than the maximum value of k_{cat} (Table 1), thus hinting at the fact that under electrocatalytic operation this general convention is oversimplified and other important factors should also be taken into account.

Table 1. Comparison of $k_{hopping}$ and k_{cat} as a Function of MeIM Concentration

MeIM concentration (mM)	$k_{hopping}$ (s^{-1})	k_{cat} (s^{-1})
0	2513	0.58
2	3858	0.83

Scheme 2 illustrates several key processes that in principle could impact the kinetics of MOF-based electrocatalysis: (1)

Scheme 2. General Illustration of the Key Processes That Govern the Overall Electrocatalytic Rates in MOF-Based Systems

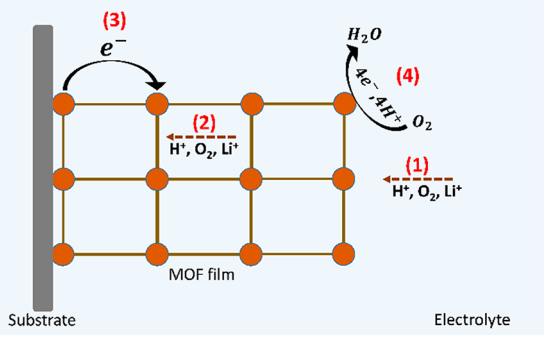

(1) - mass-transport in bulk electrolyte
(2) - mass-transport within MOF film
(3) - redox hopping rate
(4) - catalytic rate

Mass transport of bulk-solution reactants (for ORR: Li^+, H^+, and O_2) toward the MOF film. As discussed earlier, in the case of RDE-based Koutecky–Levich analysis, one can effectively eliminate this factor. (2) Mass transport of reactants (Li^+, H^+, and O_2) within the MOF's pores. As opposed to bulk solution mass transport, diffusion through the confined space in the interior of the MOF should impose a kinetic limitation even under infinite convection conditions. (3) The charge hopping rate between adjacent redox-active moieties. (4) The intrinsic catalytic rate at each MOF-anchored active site. In addition, it is important to realize that electrocatalytic proton-coupled

https://dx.doi.org/10.1021/jacs.9b11355
J. Am. Chem. Soc. 2020, 142, 1933–1940

reactions (such as ORR, H_2 evolution, CO_2 reduction, and water oxidation) entail the transfer of multiple electrons and protons in a single catalytic cycle and involve the diffusional mass transport of protons and catalytic substrates. However, $k_{hopping}$ is usually determined under noncatalytic conditions and merely measures the kinetics of a single electron transfer without any proton-based chemical steps. In other words, $k_{hopping}$ values obtained via a conventional potential-step analysis conducted under an inert atmosphere simply cannot represent the effective charge-transport kinetics during electrocatalytic operation. Thus, as an outcome of this study, future efforts to gain further understanding regarding the operation mechanisms controlling MOF-based electrocatalysis will require the development of new methods for the extraction of hopping kinetics under catalytic conditions.

CONCLUSIONS

In this work, we demonstrate that by using axial coordinative ligation one can manipulate the electronic properties of catalytically active Fe-porphyrin (Hemin) sites installed within a UIO-66 MOF film. Specifically, it was found that MeIM coordination to MOF-installed Hemins systematically tunes their electrochemical redox activity, altering the porphyrin-based $Fe^{3+/2+}$ formal potential while accelerating the rate of charge hopping between neighboring Hemin sites. Moreover, MeIM coordination also boosts the MOF's activity toward electrocatalytic ORR, significantly enhancing catalytic currents while lowering the reaction's onset potential. Furthermore, extracted catalytic ORR rates (k_{cat}) were found to be 3 orders of magnitude larger than the rate of redox hopping between adjacent MOF-installed Hemins ($k_{hopping}$). In other words, as opposed to the conventional assumption in the field, $k_{hopping}$ is not the only parameter that limits the overall electrocatalytic rate of MOF-based films. Hence, future efforts to develop efficient MOF-based electrocatalytic systems will have to consider additional key kinetic factors such as ion/proton/reactant mass transport in bulk electrolyte as well as inside the MOF's pores.

ASSOCIATED CONTENT

Supporting Information

The Supporting Information is available free of charge at https://pubs.acs.org/doi/10.1021/jacs.9b11355.

Experimental procedures, material synthesis and characterization, and additional electrochemical measurements (PDF)

AUTHOR INFORMATION

Corresponding Author

Idan Hod − *Ben-Gurion University of the Negev, Beer-Sheva, Israel;* orcid.org/0000-0003-4837-8793; Email: hodi@bgu.ac.il

Other Authors

Itamar Liberman − *Ben-Gurion University of the Negev, Beer-Sheva, Israel*

Ran Shimoni − *Ben-Gurion University of the Negev, Beer-Sheva, Israel*

Raya Ifraemov − *Ben-Gurion University of the Negev, Beer-Sheva, Israel*

Illya Rozenberg − *Ben-Gurion University of the Negev, Beer-Sheva, Israel*

Chanderpratap Singh − *Ben-Gurion University of the Negev, Beer-Sheva, Israel*

Complete contact information is available at: https://pubs.acs.org/10.1021/jacs.9b11355

Author Contributions

†These authors contributed equally.

Notes

The authors declare no competing financial interest.

ACKNOWLEDGMENTS

We thank the Ilse Katz Institute for Nanoscale Science and Technology for the technical support of material characterization. This research was supported by the Israel Science Foundation (ISF) (grant no. 306/18). R.S. is grateful for a Kreitman Ph.D. fellowship. C.S. is grateful for a Planning and Budgeting Committee (PBC) fellowship.

REFERENCES

(1) Furukawa, H.; Ko, N.; Go, Y. B.; Aratani, N.; Choi, S. B.; Choi, E.; Yazaydin, A. O.; Snurr, R. Q.; O'Keeffe, M.; Kim, J.; Yaghi, O. M. Ultrahigh Porosity in Metal-Organic Frameworks. *Science* **2010**, *329* (5990), 424−428.

(2) Furukawa, H.; Muller, U.; Yaghi, O. M. Heterogeneity within Order" in Metal-Organic Frameworks. *Angew. Chem., Int. Ed.* **2015**, *54* (11), 3417−3430.

(3) Deria, P.; Bury, W.; Hupp, J. T.; Farha, O. K. Versatile functionalization of the NU-1000 platform by solvent-assisted ligand incorporation. *Chem. Commun.* **2014**, *50* (16), 1965−1968.

(4) Farha, O. K.; Eryazici, I.; Jeong, N. C.; Hauser, B. G.; Wilmer, C. E.; Sarjeant, A. A.; Snurr, R. Q.; Nguyen, S. T.; Yazaydin, A. O.; Hupp, J. T. Metal-Organic Framework Materials with Ultrahigh Surface Areas: Is the Sky the Limit? *J. Am. Chem. Soc.* **2012**, *134* (36), 15016−15021.

(5) Kandiah, M.; Usseglio, S.; Svelle, S.; Olsbye, U.; Lillerud, K. P.; Tilset, M. Post-synthetic modification of the metal-organic framework compound UiO-66. *J. Mater. Chem.* **2010**, *20* (44), 9848−9851.

(6) Karagiaridi, O.; Bury, W.; Mondloch, J. E.; Hupp, J. T.; Farha, O. K. Solvent-Assisted Linker Exchange: An Alternative to the De Novo Synthesis of Unattainable Metal-Organic Frameworks. *Angew. Chem., Int. Ed.* **2014**, *53* (18), 4530−4540.

(7) Islamoglu, T.; Goswami, S.; Li, Z. Y.; Howarth, A. J.; Farha, O. K.; Hupp, J. T. Postsynthetic Tuning of Metal Organic Frameworks for Targeted Applications (vol 50, pg 805, 2017). *Acc. Chem. Res.* **2018**, *51* (1), 212−212.

(8) Phan, A.; Doonan, C. J.; Uribe-Romo, F. J.; Knobler, C. B.; O'Keeffe, M.; Yaghi, O. M. Synthesis, Structure, and Carbon Dioxide Capture Properties of Zeolitic Imidazolate Frameworks. *Acc. Chem. Res.* **2010**, *43* (1), 58−67.

(9) Li, J. R.; Sculley, J.; Zhou, H. C. Metal-Organic Frameworks for Separations. *Chem. Rev.* **2012**, *112* (2), 869−932.

(10) Lee, J.; Farha, O. K.; Roberts, J.; Scheidt, K. A.; Nguyen, S. T.; Hupp, J. T. Metal-organic framework materials as catalysts. *Chem. Soc. Rev.* **2009**, *38* (5), 1450−1459.

(11) Katz, M. J.; Mondloch, J. E.; Totten, R. K.; Park, J. K.; Nguyen, S. T.; Farha, O. K.; Hupp, J. T. Simple and Compelling Biomimetic Metal-Organic Framework Catalyst for the Degradation of Nerve Agent Simulants. *Angew. Chem., Int. Ed.* **2014**, *53* (2), 497−501.

(12) Li, D.; Xu, H.-Q.; Jiao, L.; Jiang, H.-L. Metal-organic frameworks for catalysis: State of the art, challenges, and opportunities. *EnergyChem.* **2019**, *1* (1), 100005.

(13) Kreno, L. E.; Leong, K.; Farha, O. K.; Allendorf, M.; Van Duyne, R. P.; Hupp, J. T. Metal-Organic Framework Materials as Chemical Sensors. *Chem. Rev.* **2012**, *112* (2), 1105−1125.

(14) Fei, H. H.; Sampson, M. D.; Lee, Y.; Kubiak, C. P.; Cohen, S. M. Photocatalytic CO_2 Reduction to Formate Using a Mn(I) Molecular Catalyst in a Robust Metal-Organic Framework. *Inorg. Chem.* **2015**, *54* (14), 6821−6828.
(15) Wang, D. K.; Huang, R. K.; Liu, W. J.; Sun, D. R.; Li, Z. H. Fe-Based MOFs for Photocatalytic CO_2 Reduction: Role of Coordination Unsaturated Sites and Dual Excitation Pathways. *ACS Catal.* **2014**, *4* (12), 4254−4260.
(16) Ahrenholtz, S. R.; Epley, C. C.; Morris, A. J. Solvothermal Preparation of an Electrocatalytic Metalloporphyrin MOF Thin Film and its Redox Hopping Charge-Transfer Mechanism. *J. Am. Chem. Soc.* **2014**, *136* (6), 2464−2472.
(17) Miner, E. M.; Fukushima, T.; Sheberla, D.; Sun, L.; Surendranath, Y.; Dinca, M. Electrochemical oxygen reduction catalysed by Ni-3(hexaiminotriphenylene)(2). *Nat. Commun.* **2016**, *7*, 7.
(18) Hod, I.; Sampson, M. D.; Deria, P.; Kubiak, C. P.; Farha, O. K.; Hupp, J. T. Fe-Porphyrin-Based Metal-Organic Framework Films as High-Surface Concentration, Heterogeneous Catalysts for Electrochemical Reduction of CO_2. *ACS Catal.* **2015**, *5* (11), 6302−6309.
(19) Hod, I.; Deria, P.; Bury, W.; Mondloch, J. E.; Kung, C. W.; So, M.; Sampson, M. D.; Peters, A. W.; Kubiak, C. P.; Farha, O. K.; Hupp, J. T. A porous proton-relaying metal-organic framework material that accelerates electrochemical hydrogen evolution. *Nat. Commun.* **2015**, *6*, 6.
(20) Kornienko, N.; Zhao, Y. B.; Kiley, C. S.; Zhu, C. H.; Kim, D.; Lin, S.; Chang, C. J.; Yaghi, O. M.; Yang, P. D. Metal-Organic Frameworks for Electrocatalytic Reduction of Carbon Dioxide. *J. Am. Chem. Soc.* **2015**, *137* (44), 14129−14135.
(21) Usov, P. M.; Huffman, B.; Epley, C. C.; Kessinger, M. C.; Zhu, J.; Maza, W. A.; Morris, A. J. Study of Electrocatalytic Properties of Metal-Organic Framework PCN-223 for the Oxygen Reduction Reaction. *ACS Appl. Mater. Interfaces* **2017**, *9* (39), 33539−33543.
(22) Liang, Z.; Zhao, R.; Qiu, T.; Zou, R.; Xu, Q. Metal-organic framework-derived materials for electrochemical energy applications. *EnergyChem.* **2019**, *1* (1), 100001.
(23) Zhu, R.; Ding, J.; Xu, Y.; Yang, J.; Xu, Q.; Pang, H. π-Conjugated Molecule Boosts Metal−Organic Frameworks as Efficient Oxygen Evolution Reaction Catalysts. *Small* **2018**, *14* (50), 1803576.
(24) Goswami, S.; Chen, M.; Wasielewski, M. R.; Farha, O. K.; Hupp, J. T. Boosting Transport Distances for Molecular Excitons within Photoexcited Metal-Organic Framework Films. *ACS Appl. Mater. Interfaces* **2018**, *10* (40), 34409−34417.
(25) Goswami, S.; Ma, L.; Martinson, A. B. F.; Wasielewski, M. R.; Farha, O. K.; Hupp, J. T. Toward Metal Organic Framework-Based Solar Cells: Enhancing Directional Exciton Transport by Collapsing Three-Dimensional Film Structures. *ACS Appl. Mater. Interfaces* **2016**, *8* (45), 30863−30870.
(26) Van Wyk, A.; Smith, T.; Park, J.; Deria, P. Charge-Transfer within Zr-Based Metal-Organic Framework: The Role of Polar Node. *J. Am. Chem. Soc.* **2018**, *140* (8), 2756−2760.
(27) Maza, W. A.; Padilla, R.; Morris, A. J. Concentration Dependent Dimensionality of Resonance Energy Transfer in a Postsynthetically Doped Morphologically Homologous Analogue of UiO-67 MOF with a Ruthenium(II) Polypyridyl Complex. *J. Am. Chem. Soc.* **2015**, *137* (25), 8161−8168.
(28) Liu, J. X.; Zhou, W. C.; Liu, J. X.; Fujimori, Y.; Higashino, T.; Imahori, H.; Jiang, X.; Zhao, J. J.; Sakurai, T.; Hattori, Y.; Matsuda, W.; Seki, S.; Garlapati, S. K.; Dasgupta, S.; Redel, E.; Sunag, L. C.; Woll, C. A new class of epitaxial porphyrin metal-organic framework thin films with extremely high photocarrier generation efficiency: promising materials for all-solid-state solar cells. *J. Mater. Chem. A* **2016**, *4* (33), 12739−12747.
(29) Liu, J. X.; Zhou, W. C.; Liu, J. X.; Howard, I.; Kilibarda, G.; Schlabach, S.; Coupry, D.; Addicoat, M.; Yoneda, S.; Tsutsui, Y.; Sakurai, T.; Seki, S.; Wang, Z. B.; Lindemann, P.; Redel, E.; Heine, T.; Woll, C. Photoinduced Charge-Carrier Generation in Epitaxial MOF Thin Films: High Efficiency as a Result of an Indirect Electronic Band Gap? *Angew. Chem., Int. Ed.* **2015**, *54* (25), 7441−7445.
(30) Ifraemov, R.; Shimoni, R.; He, W.; Peng, G.; Hod, I. A metal−organic framework film with a switchable anodic and cathodic behaviour in a photo-electrochemical cell. *J. Mater. Chem. A* **2019**, *7* (7), 3046−3053.
(31) Furukawa, H.; Cordova, K. E.; O'Keeffe, M.; Yaghi, O. M. The Chemistry and Applications of Metal-Organic Frameworks. *Science* **2013**, *341* (6149), 1230444.
(32) Wang, C.; Xie, Z. G.; de Krafft, K. E.; Lin, W. L. Doping Metal-Organic Frameworks for Water Oxidation, Carbon Dioxide Reduction, and Organic Photocatalysis. *J. Am. Chem. Soc.* **2011**, *133* (34), 13445−13454.
(33) Zhang, T.; Lin, W. B. Metal-organic frameworks for artificial photosynthesis and photocatalysis. *Chem. Soc. Rev.* **2014**, *43* (16), 5982−5993.
(34) Kornienko, N.; Zhao, Y.; Kley, C. S.; Zhu, C.; Kim, D.; Lin, S.; Chang, C. J.; Yaghi, O. M.; Yang, P. Metal−organic frameworks for electrocatalytic reduction of carbon dioxide. *J. Am. Chem. Soc.* **2015**, *137* (44), 14129−14135.
(35) Ye, L.; Liu, J.; Gao, Y.; Gong, C.; Addicoat, M.; Heine, T.; Wöll, C.; Sun, L. Highly oriented MOF thin film-based electrocatalytic device for the reduction of CO_2 to CO exhibiting high faradaic efficiency. *J. Mater. Chem. A* **2016**, *4* (40), 15320−15326.
(36) Kung, C. W.; Otake, K.; Buru, C. T.; Goswami, S.; Cui, Y. X.; Hupp, J. T.; Spokoyny, A. M.; Farha, O. K. Increased Electrical Conductivity in a Mesoporous Metal-Organic Framework Featuring Metallacarboranes Guests. *J. Am. Chem. Soc.* **2018**, *140* (11), 3871−3875.
(37) Goswami, S.; Ray, D.; Otake, K.; Kung, C. W.; Garibay, S. J.; Islamoglu, T.; Atilgan, A.; Cui, Y. X.; Cramer, C. J.; Farha, O. K.; Hupp, J. T. A porous, electrically conductive hexa-zirconium (IV)metal-organic framework. *Chem. Sci.* **2018**, *9* (19), 4477−4482.
(38) Talin, A. A.; Centrone, A.; Ford, A. C.; Foster, M. E.; Stavila, V.; Haney, P.; Kinney, R. A.; Szalai, V.; El Gabaly, F.; Yoon, H. P.; Leonard, F.; Allendorf, M. D. Tunable Electrical Conductivity in Metal-Organic Framework Thin-Film Devices. *Science* **2014**, *343* (6166), 66−69.
(39) Sheberla, D.; Sun, L.; Blood-Forsythe, M. A.; Er, S.; Wade, C. R.; Brozek, C. K.; Aspuru-Guzik, A.; Dinca, M. High Electrical Conductivity in Ni-3(2,3,6,7,10,11-hexaiminotriphenylene)(2), a Semiconducting Metal-Organic Graphene Analogue. *J. Am. Chem. Soc.* **2014**, *136* (25), 8859−8862.
(40) Wang, T. C.; Hod, I.; Audu, C. O.; Vermeulen, N. A.; Nguyen, S. T.; Farha, O. K.; Hupp, J. T. Rendering High Surface Area, Mesoporous Metal−Organic Frameworks Electronically Conductive. *ACS Appl. Mater. Interfaces* **2017**, *9* (14), 12584−12591.
(41) Wade, C. R.; Li, M. Y.; Dinca, M. Facile Deposition of Multicolored Electrochromic Metal-Organic Framework Thin Films. *Angew. Chem., Int. Ed.* **2013**, *52* (50), 13377−13381.
(42) Hod, I.; Bury, W.; Gardner, D. M.; Deria, P.; Roznyatovskiy, V.; Wasielewski, M. R.; Farha, O. K.; Hupp, J. T. Bias-Switchable Permselectivity and Redox Catalytic Activity of a Ferrocene-Functionalized, Thin-Film Metal-Organic Framework Compound. *J. Phys. Chem. Lett.* **2015**, *6* (4), 586−591.
(43) D'Alessandro, D. M. Exploiting redox activity in metal-organic frameworks: concepts, trends and perspectives. *Chem. Commun.* **2016**, *52* (58), 8957−8971.
(44) Hod, I.; Farha, O. K.; Hupp, J. T. Modulating the rate of charge transport in a metal-organic framework thin film using host: guest chemistry. *Chem. Commun.* **2016**, *52* (8), 1705−1708.
(45) Maindan, K.; Li, X.; Yu, J.; Deria, P. Controlling Charge-Transport in Metal−Organic Frameworks: Contribution of Topological and Spin-State Variation on the Iron−Porphyrin Centered Redox Hopping Rate. *J. Phys. Chem. B* **2019**, *123* (41), 8814−8822.
(46) Scheidt, W. R.; Reed, C. A. Spin-state/stereochemical relationships in iron porphyrins: implications for the hemoproteins. *Chem. Rev.* **1981**, *81* (6), 543−555.
(47) Shimoni, R.; He, W.; Liberman, I.; Hod, I. Tuning of Redox Conductivity and Electrocatalytic Activity in Metal−Organic Frame-

https://dx.doi.org/10.1021/jacs.9b11355
J. Am. Chem. Soc. 2020, 142, 1933−1940

work Films Via Control of Defect Site Density. *J. Phys. Chem. C* **2019**, *123* (9), 5531−5539.
(48) Katz, M. J.; Brown, Z. J.; Colon, Y. J.; Siu, P. W.; Scheidt, K. A.; Snurr, R. Q.; Hupp, J. T.; Farha, O. K. A facile synthesis of UiO-66, UiO-67 and their derivatives. *Chem. Commun.* **2013**, *49* (82), 9449−9451.
(49) Deria, P.; Mondloch, J. E.; Tylianakis, E.; Ghosh, P.; Bury, W.; Snurr, R. Q.; Hupp, J. T.; Farha, O. K. Perfluoroalkane Functionalization of NU-1000 via Solvent-Assisted Ligand Incorporation: Synthesis and CO_2 Adsorption Studies. *J. Am. Chem. Soc.* **2013**, *135* (45), 16801−16804.
(50) Sun, Y.; Sun, L.; Feng, D.; Zhou, H.-C. An In Situ One-Pot Synthetic Approach towards Multivariate Zirconium MOFs. *Angew. Chem., Int. Ed.* **2016**, *55* (22), 6471−6475.
(51) Øien, S.; Wragg, D.; Reinsch, H.; Svelle, S.; Bordiga, S.; Lamberti, C.; Lillerud, K. P. Detailed Structure Analysis of Atomic Positions and Defects in Zirconium Metal−Organic Frameworks. *Cryst. Growth Des.* **2014**, *14* (11), 5370−5372.
(52) Ma, X.; Wang, L.; Zhang, Q.; Jiang, H.-L. Switching on the Photocatalysis of Metal−Organic Frameworks by Engineering Structural Defects. *Angew. Chem.* **2019**, *131* (35), 12303−12307.
(53) Atzori, C.; Shearer, G. C.; Maschio, L.; Civalleri, B.; Bonino, F.; Lamberti, C.; Svelle, S.; Lillerud, K. P.; Bordiga, S. Effect of Benzoic Acid as a Modulator in the Structure of UiO-66: An Experimental and Computational Study. *J. Phys. Chem. C* **2017**, *121* (17), 9312−9324.
(54) Burke, J. M.; Kincaid, J. R.; Peters, S.; Gagne, R. R.; Collman, J. P.; Spiro, T. G. Structure-Sensitive Resonance Raman Bands of Tetraphenyl and Picket Fence Porphyrin-Iron Complexes, Including an Oxyhemoglobin Analog. *J. Am. Chem. Soc.* **1978**, *100* (19), 6083−6088.
(55) Hirst, J.; Wilcox, S. K.; Ai, J.; Moënne-Loccoz, P.; Loehr, T. M.; Goodin, D. B. Replacement of the Axial Histidine Ligand with Imidazole in Cytochrome c Peroxidase. 2. Effects on Heme Coordination and Function. *Biochemistry* **2001**, *40* (5), 1274−1283.
(56) Huang, W.; Hao, Q.; Lei, W.; Wu, L.; Xia, X. J. M. R. E. Polypyrrole-hemin-reduce graphene oxide: rapid synthesis and enhanced electrocatalytic activity towards the reduction of hydrogen peroxide. *Mater. Res. Express* **2014**, *1* (4), 045601.
(57) Nesset, M. J. M.; Shokhirev, N. V.; Enemark, P. D.; Jacobson, S. E.; Walker, F. A. Models of the cytochromes. Redox properties and thermodynamic stabilities of complexes of "hindered" iron(III) and iron(II) tetraphenylporphyrinates with substituted pyridines and imidazoles. *Inorg. Chem.* **1996**, *35* (18), 5188−5200.
(58) Daum, P.; Murray, R. W. Chemically Modified Electrodes. 29. Charge-Transfer Diffusion Rates and Activity Relationships during Oxidation and Reduction of Plasma-Polymerized Vinylferrocene Films. *J. Phys. Chem.* **1981**, *85* (4), 389−396.
(59) Pegis, M. L.; McKeown, B. A.; Kumar, N.; Lang, K.; Wasylenko, D. J.; Zhang, X. P.; Raugei, S.; Mayer, J. M. Homogenous Electrocatalytic Oxygen Reduction Rates Correlate with Reaction Overpotential in Acidic Organic Solutions. *ACS Cent. Sci.* **2016**, *2* (11), 850−856.
(60) Zeng, Z. Y.; Gupta, S. L.; Huang, H.; Yeager, E. B. Oxygen reduction on poly(4-vinylpyridine)-modified ordinary pyrolytic graphite electrodes with adsorbed cobalt tetra-sulphonated phthalocyanine in acid solutions. *J. Appl. Electrochem.* **1991**, *21* (11), 973−981.
(61) Scott, S. M.; Gordon, K. C.; Burrell, A. K. Spectroelectrochemical Studies of Copper(I) Complexes with Binaphthyridine and Biquinoline Ligands. Crystal Structure Determination of Bis(6,7-dihydrodipyrido[2,3-b:3',2'-j][1,10]phenanthroline)copper(I) Tetrafluoroborate. *Inorg. Chem.* **1996**, *35* (9), 2452−2457.
(62) Pegis, M. L.; Martin, D. J.; Wise, C. F.; Brezny, A. C.; Johnson, S. I.; Johnson, L. E.; Kumar, N.; Raugei, S.; Mayer, J. M. Mechanism of Catalytic O_2 Reduction by Iron Tetraphenylporphyrin. *J. Am. Chem. Soc.* **2019**, *141* (20), 8315−8326.
(63) Ramos Sende, J. A.; Arana, C. R.; Hernandez, L.; Potts, K. T.; Keshevarz-K, M.; Abruna, H. D. Electrocatalysis of CO_2 Reduction in Aqueous Media at Electrodes Modified with Electropolymerized Films of Vinylterpyridine Complexes of Transition Metals. *Inorg. Chem.* **1995**, *34* (12), 3339−3348.

https://dx.doi.org/10.1021/jacs.9b11355
J. Am. Chem. Soc. 2020, 142, 1933−1940